

Electronic Supplementary Information (ESI)

Bifunctional in-situ polymerized nanocomposites for convective solar desalination and enhanced photo-thermoelectric power generation

Muhammad Sultan Irshad^a, Xianbao Wang^{a, *}, Naila Arshad^b, M. Qasim Javed^c, Tariq Shamim^d,
Zhenzhen Guo^a, Hong Rong Li^b, Jianying Wang^a, and Tao Mei^a

^aMinistry of Education Key Laboratory for the Green Preparation and Application of Functional Materials, Collaborative Innovation Center for Advanced Organic Chemical Materials Co-constructed by the Province and Ministry, Hubei Key Laboratory of Polymer Materials (Hubei University), School of Materials Science and Engineering, Hubei University, Wuhan 430062, P.R. China.

^bInstitute of Quantum Optics and Quantum Information, School of Science, Xi'an Jiaotong University, (XJTU), Xi'an 710049, China.

^cFood and Biotechnology Research Center (FBRC), Pakistan Council of Scientific and Industrial Research, Lahore, (54000), Pakistan.

^dDepartment of Mechanical Engineering, Northern Illinois University, 590 Garden Road, DeKalb, Illinois 60115, USA

* Corresponding author. Tel.: +86-2788661729; Fax: +86-2788661729.

Email: wangxb68@aliyun.com (X.B. Wang)

Contents

Figure S1. FESEM image of the honeycomb-like structure of MnO ₂ @PPy.....	3
.....	3
Figure S2. XPS survey of pure MnO ₂ NWs, and in-situ polymerized MnO ₂ @PPy.....	3
Figure S3. A salt-resistant and heat accumulated evaporating structure.	4
Note S1. The ratio of wicks to evaporation area	4
Figure S4. COMSOL Multiphysics heat transfer simulations performed based on experimentally measured parameters	5
Note S2. Computational Fluid Dynamic Simulation (CFDs)	6
Figure S5. The temperature distribution through the wick region for two different concentrations at the top surface: $Ch = 5\%$ and $Ch = 25\%$ in perpendicularly oriented regions (W-W section).	7
Figure S7. The surface temperature of four developed evaporating systems e.g., pure water, polyurethane foam, pure MnO ₂ NWs, and in-situ polymerized MnO ₂ @PPy NCs.	9
Figure S8. Time-dependent mass change under different solar intensities up to 3 kW m ⁻²	9
Note.S3 Photothermal conversion calculations	10
S3.1 Heat losses.....	11
S3.1.1 Conductive heat loss	11
S3.1.2 Convective heat loss.....	11
S3.1.3 Radiative heat loss	12
Figure S9. Long-term evaporation efficiency of MnO ₂ @PPy solar evaporator under intense solar Intensity (3 kW m ⁻²) for continuous 6 hr using stimulated seawater (3.5 wt%, NaCl).	13
Note S4. Outdoor experiment details	13
Figure S10. IR image of MnO ₂ @PPy based photo-thermoelectric generators under 1 kW m ⁻² and without light irradiance.	14
Reference	14

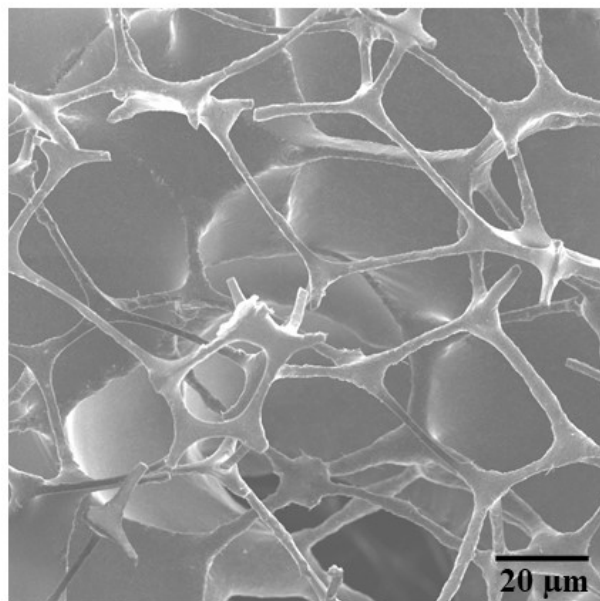


Figure S1. FESEM image of the honeycomb-like structure of MnO₂@PPy.

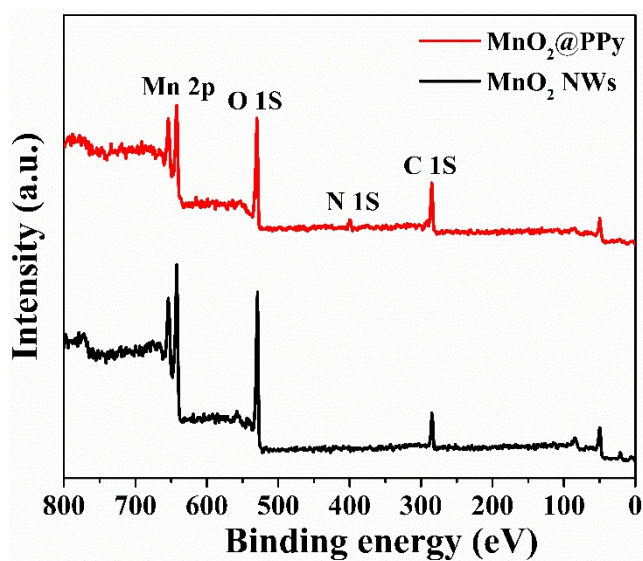


Figure S2. XPS survey of pure MnO₂ NWs, and in-situ polymerized MnO₂@PPy.

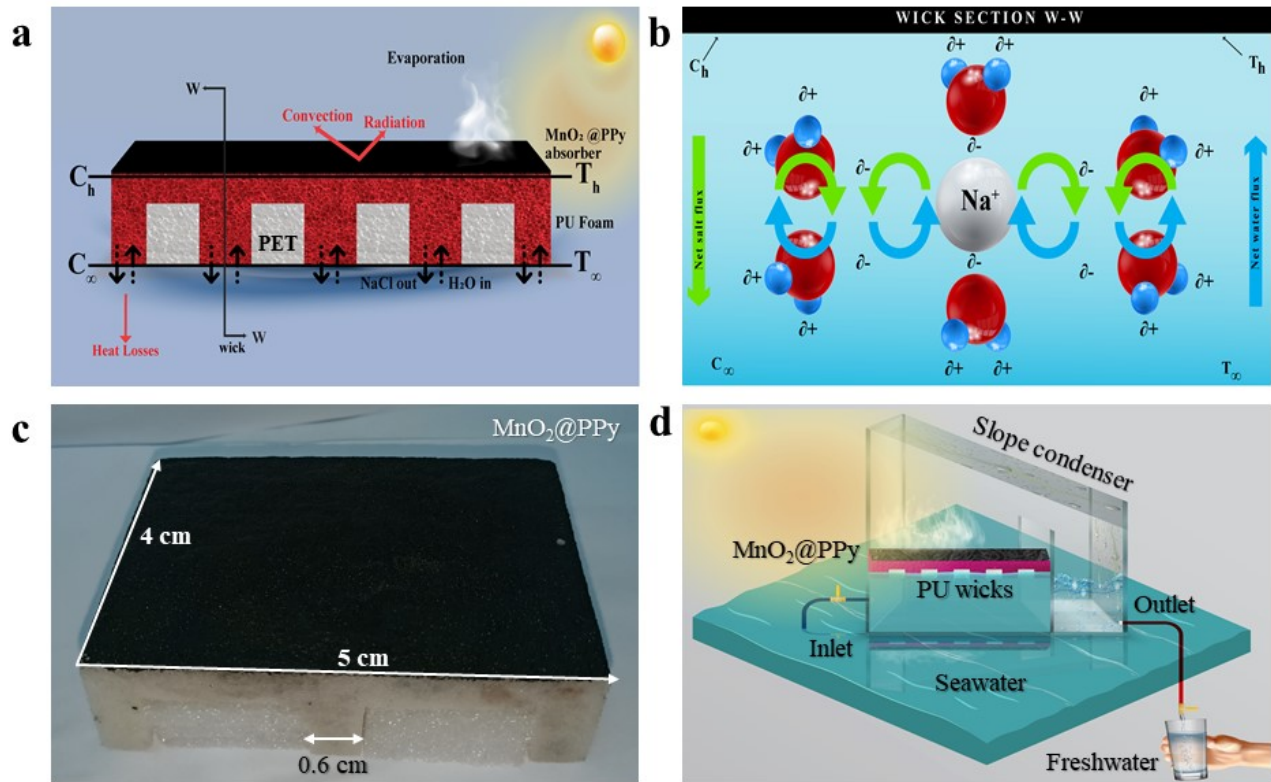


Figure S3. A salt-resistant and heat accumulated evaporating structure. (a) schematic illustration of salinity gradient convection model composed of in-situ polymerized MnO₂@PPy evaporator coated on two-phase crafted polyurethane wicks where hot brine and water flows via chemical convection process and PET foam provides thermal insulation and restricts hot brine mass flux into wicks channels only. (b) demonstrates the salinity gradient between denser surface salts and bulk seawater. (c) optical image of MnO₂@PPy solar evaporating structure. (d) schematic illustration of outdoor MnO₂@PPy prototype along with glass slope condenser floating on seawater.

Note S1. The ratio of wicks to evaporation area

$$\begin{aligned} \text{The volume of one polyurethane wick} &= 0.6 \text{ cm} \times 4 \text{ cm} \times 2 \text{ cm} \\ &= 4.2 \text{ cm}^3 \end{aligned}$$

$$\begin{aligned} \text{The area of one polyurethane wick} &= 0.6 \text{ cm} \times 4 \text{ cm} \\ &= 2.4 \text{ cm}^2 \end{aligned}$$

$$\text{The area of three polyurethane wick} = 2.4 \text{ cm}^2 \times 3$$

$$= 7.2 \text{ cm}^2$$

The total area of $\text{MnO}_2@\text{PPy}$ evaporation layer = $5 \text{ cm} \times 4 \text{ cm}$

$$= 20 \text{ cm}^2$$

The ratio of three wicks / $\text{MnO}_2@\text{PPy}$ evaporation layer (%) = $\frac{7.2 \text{ cm}^2}{20 \text{ cm}^2} \times 100$

$$= 36 \%$$

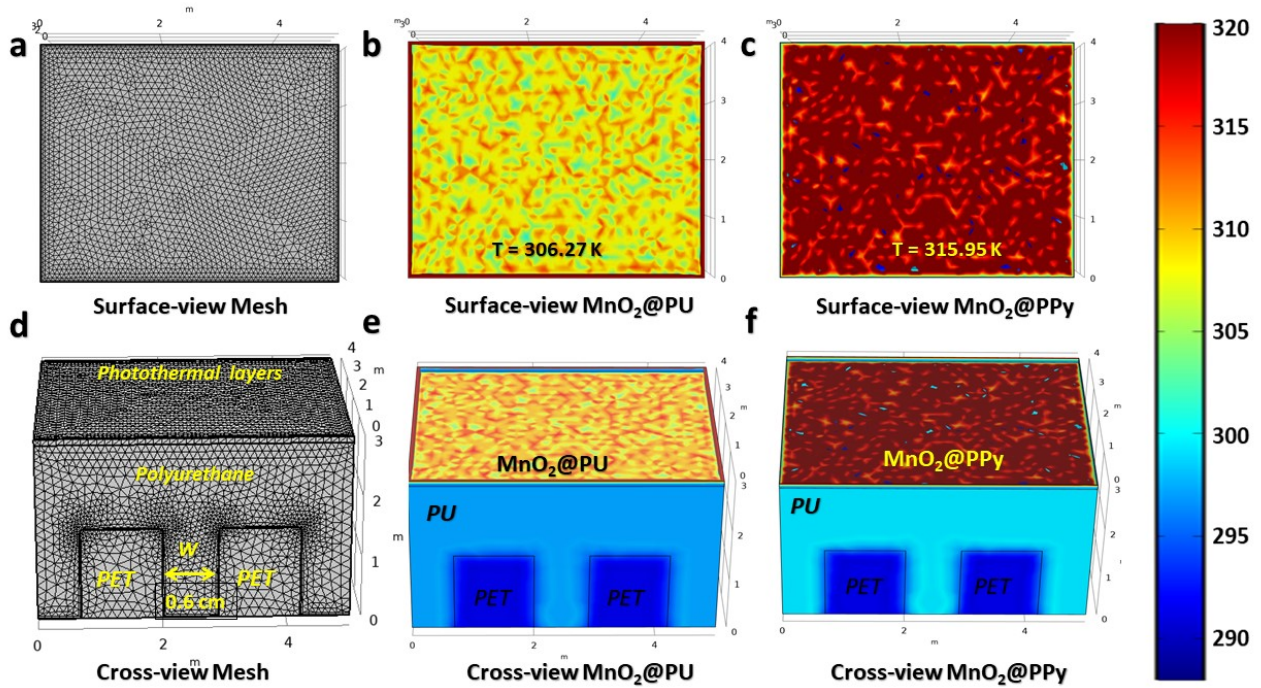


Figure S4. COMSOL Multiphysics heat transfer simulations performed based on experimentally measured parameters e.g., materials selection with their respective geometry and surface temperatures, etc. **(a)** Geometrical dimensions of surface mesh ($4 \text{ cm} \times 5 \text{ cm} = 20 \text{ cm}^2$) of salt-resistant evaporating structure. **(b-c)** Surface view of MnO_2 NWs@PU foam represents average surface temperature while in-situ polymerized $\text{MnO}_2@\text{PPy}$ owes diffuse reflection that enhanced its solar absorption and sustains enough surface temperature (315.95 K) to evaporate vapors efficiently. **(d)** Shows complete cross-view mesh geometry of salt-resistant in-situ polymerized MnO_2 NWs deposited over two-phase localized polyurethane wicks and an insulating polystyrene terephthalate barrier. **(e-f)** Cross-view images of both MnO_2 NWs@PU and $\text{MnO}_2@\text{PPy}$ solar evaporator denotes the heat accumulation at the top interface, the inclusion of PET thermal barrier restricts heat transfer to underneath bulk water.

Note S2. Computational Fluid Dynamic Simulation (CFDs)

COMSOL Multiphysics 5.5 was employed to simulate a single wick to examine the fluid flowing pattern, salt transportation, and heat flux dispersion. The 3D Finite Volume Method (FVM) was applied to numerically compute momentum, energy, and salt transportation (convection) for a single wick to derive the temperature and velocity perturbations throughout the region¹. The wick was simulated as a tube filled with a specific concentration of the saltwater solution, as demonstrated in Figure 5a. The model was simulated with closed walls on both sides, impermeable to any flow (heat and fluid). The upper and lower walls were simulated to be permeable to fluid flow and heat flux. Besides, the local salt concentration along with temperature for top and bottom openings were selected to be constant. All of the four sides were simulated with no-slip boundary conditions. For thermal transport through the single-wick domain, natural convection and conduction mechanism were opted (as a result of concentration gradient).

Setting the condition of laminar and steady-state flow condition for the fluid while neglecting the viscosity perturbation, the Navier-Stokes equations can be transformed as^{2,3}:

$$\frac{\partial(\rho u)}{\partial x} + \frac{\partial(\rho v)}{\partial y} + \frac{\partial(\rho w)}{\partial z} = 0 \dots\dots\dots(1)$$

$$\frac{\partial(\rho u u)}{\partial x} + \frac{\partial(\rho u v)}{\partial y} + \frac{\partial(\rho u w)}{\partial z} = \frac{\partial P}{\partial x} + \mu \left(\frac{\partial^2 u}{\partial x^2} + \frac{\partial^2 u}{\partial y^2} + \frac{\partial^2 u}{\partial z^2} \right) \dots\dots\dots(2)$$

$$\frac{\partial(\rho v u)}{\partial x} + \frac{\partial(\rho v v)}{\partial y} + \frac{\partial(\rho v w)}{\partial z} = \frac{\partial P}{\partial y} + \mu \left(\frac{\partial^2 v}{\partial x^2} + \frac{\partial^2 v}{\partial y^2} + \frac{\partial^2 v}{\partial z^2} \right) \dots\dots\dots(3)$$

$$\frac{\partial(\rho u w)}{\partial x} + \frac{\partial(\rho v w)}{\partial y} + \frac{\partial(\rho w w)}{\partial z} = \frac{\partial P}{\partial z} + \mu \left(\frac{\partial^2 w}{\partial x^2} + \frac{\partial^2 w}{\partial y^2} + \frac{\partial^2 w}{\partial z^2} \right) - \rho g [1 - \beta (T - T_\infty)] \dots\dots(4)$$

Where β presents the volumetric thermal expansion, T_∞ denotes the reference temperature being operated.

For liquid, the energy equation can be given as:

$$\rho C_p \left(u \frac{\partial T}{\partial x} + v \frac{\partial T}{\partial y} + w \frac{\partial T}{\partial z} \right) = k \left(\frac{\partial^2 T}{\partial x^2} + \frac{\partial^2 T}{\partial y^2} + \frac{\partial^2 T}{\partial z^2} \right) \dots \dots \dots (5)$$

By resolving the convection equation of salt concentration, the local salt mass fraction can be computed:

$$\frac{\partial(\rho u C)}{\partial x} + \frac{\partial(\rho v C)}{\partial y} + \frac{\partial(\rho w C)}{\partial z} = \frac{\partial(\rho D \frac{\partial C}{\partial x})}{\partial x} + \frac{\partial(\rho D \frac{\partial C}{\partial y})}{\partial y} + \frac{\partial(\rho D \frac{\partial C}{\partial z})}{\partial z} \dots \dots \dots (6)$$

It is worthy to note that ρ presents the density of the liquid (salty water) which varies spatially.

The temperature distribution through the wick region for two different concentrations at the top surface: $C_h = 5\%$ and $C_h = 25\%$ in perpendicularly oriented regions (W-W section) is illustrated in **Figure S5**. The simulated outcomes exhibit that for the low concentration, the W-W plane reveals a uniform distribution of temperature is observed along y-direction while for the high concentrations, a periodic temperature distribution is observed. For each boundary condition, these temperature distributive outcomes were employed to compute the heat flux for the wick region (accordingly to wick area), and the resulting data is shown in Figure 6. Although convection has a contribution to salt- rejecting, the prominent mechanism for heat transportation is conductive at a lower concentration. Upon enhancing the salt concentration up to 25%, salt concentration gradient (density gradient) induces natural convection and stimulates heat transportation.

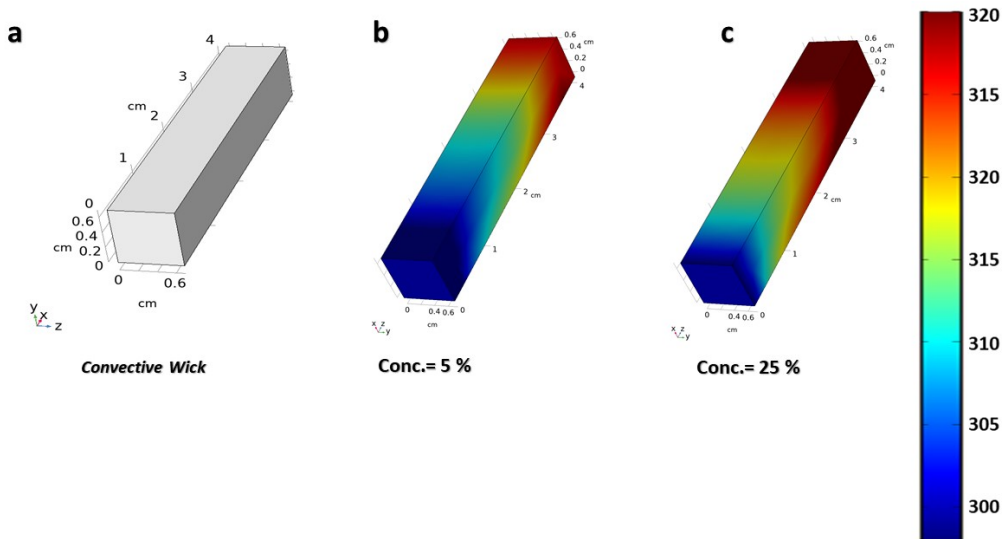


Figure S5. The temperature distribution through the wick region for two different concentrations at the top surface: $C_h = 5\%$ and $C_h = 25\%$ in perpendicularly oriented regions (W-W section).

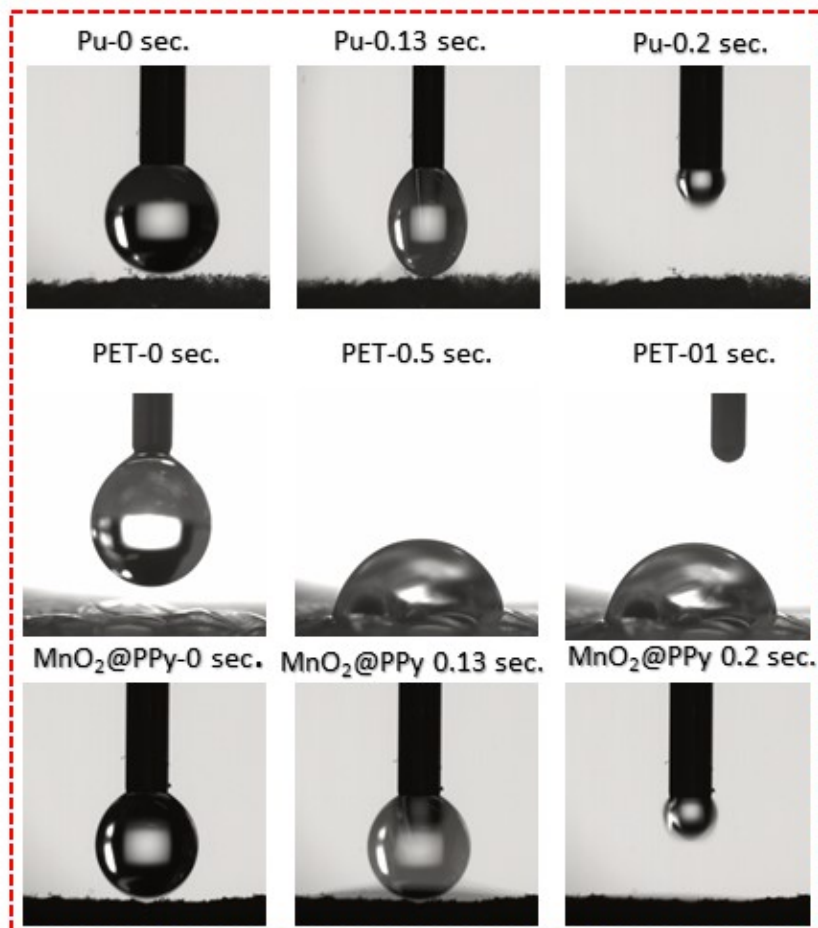


Figure S6. Contact angle test of pure polyurethane foam (PU), polyurethane terephthalate (PET), and in-situ polymerized MnO₂@PPy solar evaporator.

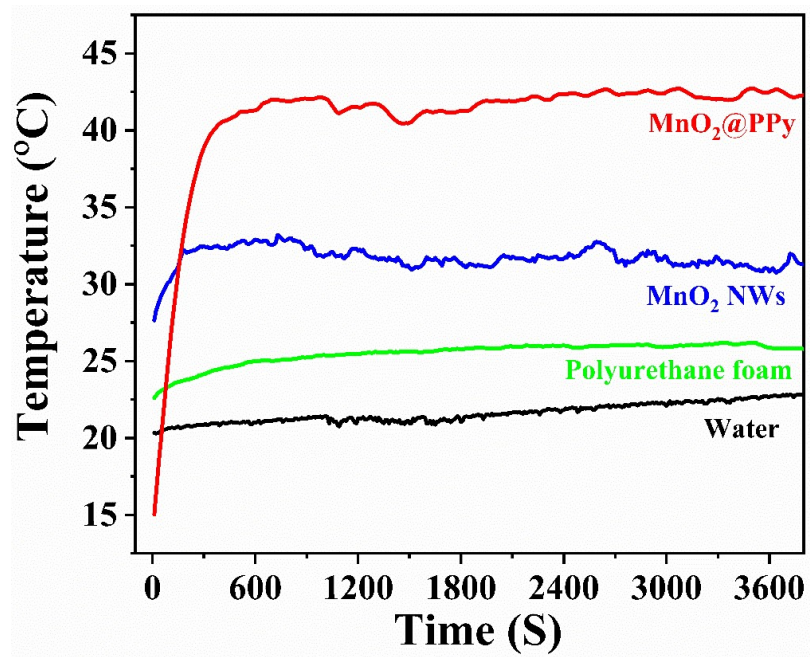


Figure S7. The surface temperature of four developed evaporating systems e.g., pure water, polyurethane foam, pure MnO₂ NWs, and in-situ polymerized MnO₂@PPy NCs.

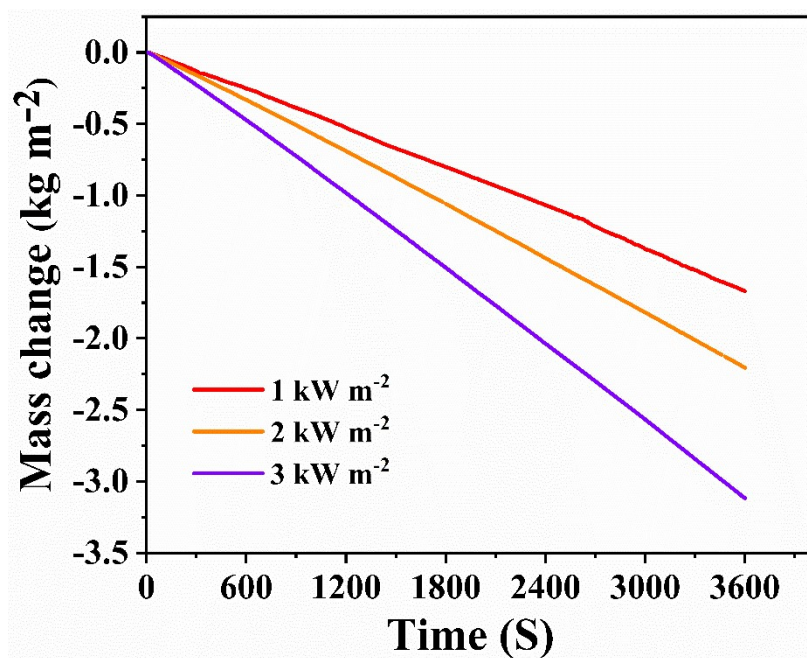


Figure S8. Time-dependent mass change under different solar intensities up to 3 kW m⁻².

Note.S3 Photothermal conversion calculations

The photothermal energy conversion efficiency (η) for the salt-resistive MnO₂@PPy solar evaporator was derived by the following equations⁴.

$$\eta_{evap} = \frac{\dot{m}_v h_{LV}}{q_i} \dots\dots\dots(7)$$

$$h_{LV} = \kappa + C \Delta T \dots\dots\dots(8)$$

Where \dot{m}_v shows evaporation rate (1.69 kg m⁻² h⁻¹) under solar irradiance excluding evaporation rate of pure water (mass flux), h_{LV} represents total enthalpy of liquid to vapor phase change including sensible

heat and phase enthalpy change, q_{solar} is the incident solar energy (1 kW m^{-2}). The λ belongs to the latent heat of phase change while it varies at different temperatures ($2430 \text{ kJ kg}^{-1} \text{ K}^{-1}$ at $30 \text{ }^\circ\text{C}$, and $2256 \text{ kJ kg}^{-1} \text{ K}^{-1}$ at $100 \text{ }^\circ\text{C}$). However, C is the specific heat capacity of water ($4.2 \text{ kJ kg}^{-1} \text{ K}^{-1}$) while ΔT represents the gradual increase of water temperature. The humidity was recorded at 44% approximately, and the environment temperature was $22.5 \pm 1 \text{ }^\circ\text{C}$ during solar-driven experiments. Following these above equations, $\text{MnO}_2@\text{PPy}$ can generate vapor at $42.8 \text{ }^\circ\text{C}$ with the corresponding photothermal conversion efficiency (88.1%) excluding evaporation rate measured in dark to insulate the precise effect of solar input, and heat conduction losses, etc.

$$\eta_{evap} = \frac{1.69 \times 2256 \text{ kJ kg}^{-1} \text{ K}^{-1}}{1 \times 3600} \times 100 \% \dots\dots\dots(9)$$

$$\eta_{evap} = 105.90 \% \dots\dots\dots(10)$$

Pure water evaporation rate efficiency = 11.9%

$$\eta_{evap} = (105.90 - 11.9) \% = 94.00 \% \dots\dots\dots(11)$$

Total heat losses = 5.90%

$$\eta_{evap} = (94.00 - 5.90) \% = 88.1 \% \dots\dots\dots(12)$$

Consequently, water absorbed the surrounding heat which increased the vapor production rate while the whole system floated in water under incident light. Thus, the total heat losses were approximately 5.90% , corresponding to the accurate evaporation rate (88.1%) of the $\text{MnO}_2@\text{PPy}$ solar evaporating system.

S3.1 Heat losses

In order to evaluate the exact photothermal conversion efficiency of $\text{MnO}_2@\text{PPy}$ solar evaporator, the heat conduction losses were assessed in terms of heat transfer to bulk water ($Q_{\text{Conduction}}$), convective heat transfer into the air ($Q_{\text{Convection}}$), and heat transfer into surrounding ($Q_{\text{Radiation}}$), as illustrated below. The thermal transport theory was applied for photothermal conversion phenomena under solar irradiance (1 kW m^{-2}).

S3.1.1 Conductive heat loss

The conductive ($Q_{\text{Conduction}}$) heat transfer into bulk water for $\text{MnO}_2@\text{PPy}$ solar evaporator was assessed by the following equation:

$$Q_{\text{Conduction}} = Ak \frac{(T_1 - T_2)}{\Delta l} \dots\dots\dots(13)$$

where A represents the cross-sectional area (16.9 mm^2), k denotes the heat conduction for underlying water ($0.6 \text{ W m}^{-1} \text{ K}^{-1}$). The water temperature was recorded by employing two embedded thermocouples with an intermediate distance of 5 mm (Δl). The temperature of the water was analyzed at a different time under consistent solar irradiance. At point 1 over, the average temperature after one hour is almost $22.7 \text{ }^\circ\text{C}$. At point 2, the average temperature over one hour is almost $22.0 \text{ }^\circ\text{C}$, approximately. Consequently, the conductive heat loss ($Q_{\text{Conduction}}$) was calculated to be 23.66 W m^{-2} , giving the 2.366 %.

S3.1.2 Convective heat loss

To account for the heat dissipation during solar evaporation in the form of convective heat loss ($Q_{\text{Convection}}$), the following equation utilized:

$$Q_{\text{convection}} = h (T_s - T_v) \dots\dots\dots(14)$$

where h presents the convective heat transport coefficient (approximately $10 \text{ W m}^{-2} \text{ K}^{-1}$), T_s presents the upper layer temperature of evaporating device ($42.8 \text{ }^\circ\text{C}$). The surrounding environmental temperature can reach up to $39.8 \text{ }^\circ\text{C}$ due to hot vapor production. Consequently, the convective heat loss ($Q_{\text{Convection}}$) came out to be 30.0 W m^{-2} , indicating a 3.0 % value.

S3.1.3 Radiative heat loss

The following equation was applied to analyze the radiative heat losses ($Q_{\text{Radiation}}$):

$$Q_{\text{Radiation}} = \varepsilon \sigma (T_s^4 - T_\infty^4) \dots\dots\dots(15)$$

where ϵ represents the emission of the absorber (assumed to be 0.93), σ denotes the Stefan-Boltzmann constant ($5.669 \times 10^{-8} \text{ W m}^{-2} \text{ K}^{-4}$), T_{∞} presents the adjacent environment temperature. As the surface is occupied by vapors that are semi-transparent to thermal radiation, so thermal wastage could be delimited due to radiative heat loss by maximum and minimum values computed by $T_{\infty} = T_a$ (ambient temperature of $22.7 \text{ }^{\circ}\text{C}$) and $T_{\infty} = T_v$ (vapor temperature of $39.8 \text{ }^{\circ}\text{C}$), respectively

When $T_{\infty} = T_a = 22.7 \text{ }^{\circ}\text{C}$, the radiative heat loss is computed to be 4.70 W m^{-2} , corresponding to 0.47% .

When $T_{\infty} = T_v = 48.5 \text{ }^{\circ}\text{C}$, the radiative heat loss is computed to be 5.40 W m^{-2} , corresponding to 0.54% .

Therefore, in the presented work, the radiative heat loss meets in the range of $0.47 \sim 0.54 \%$.

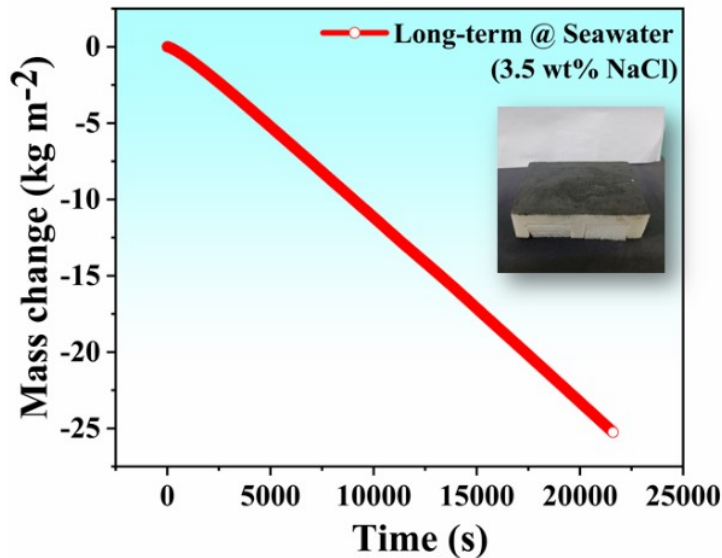


Figure S9. Long-term evaporation efficiency of $\text{MnO}_2@\text{PPy}$ solar evaporator under intense solar Intensity (3 kW m^{-2}) for continuous 6 hr using stimulated seawater (3.5 wt%, NaCl).

Note S4. Outdoor experiment details

To diversify our evaporating system, specific stimulated seawater collection was formulated. The collected stimulated seawater poured into a glass slope bipartition-based prototype as demonstrated in Figure 1d. The successive pouring of stimulated seawater was carried out during the whole day. The

Hukseflux LP-02 thermal pyranometer was employed to measure the solar intensity during the whole day. The advanced electronic analytical balance (Mettler Toledo, ME204) fortified with 0.001 g resolution was employed to compute mass variation investigations during the whole day. Indeed, mass variation along with corresponding surface temperature (FLIR I.R Camera) was noted, humidity, and collected amount of water also monitored throughout the day from 10:00 am to 4:00 pm.

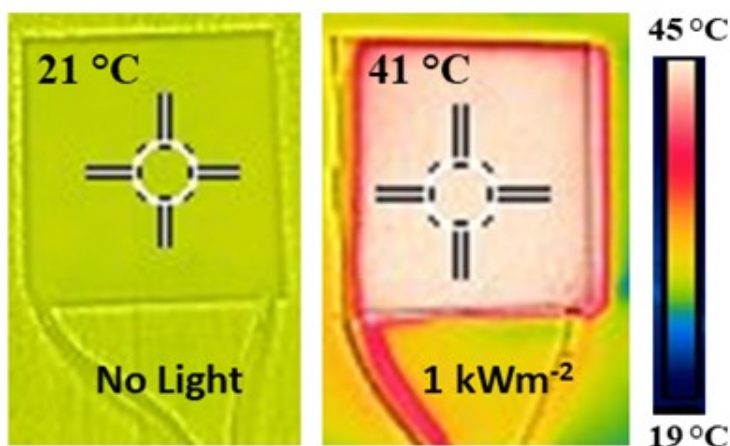


Figure S10. IR image of MnO₂@PPy based photo-thermoelectric generators under 1 kW m⁻² and without light irradiance.

Reference

- 1 R. J. Clark and S. O. Bade Shrestha, in *49th AIAA/ASME/SAE/ASEE Joint Propulsion Conference*, 2013, p. 3724.
- 2 G. Ni, S. H. Zandavi, S. M. Javid, S. V Boriskina, T. A. Cooper and G. Chen, A salt-rejecting floating solar still for low-cost desalination, *Energy Environ. Sci.*, 2018, **11**, 1510–1519.
- 3 S. Jamshed, *Using HPC for Computational Fluid Dynamics: A guide to high performance computing for CFD engineers*, Academic Press, 2015.
- 4 M. S. Irshad, X. Wang, A. Abbas, F. Yu, J. Li, J. Wang, T. Mei, J. Qian, S. Wu and M. Q. Javed, Salt-resistant carbon dots modified solar steam system enhanced by chemical advection, *Carbon N. Y.*, , DOI:10.1016/j.carbon.2021.01.140.

